Article

Ruthenium-Substituted Polyoxoanion Serves as Redox Shuttle and Intermediate Stabilizer in Selective Electrooxidation of Ethylene to Ethylene Glycol

Jiaqi Yu,[♦] Charles Bruce Musgrave, III,[♦] Qiucheng Chen,[♦] Yi Yang, Cong Tian, Xiaobing Hu, Guangcan Su, Heejong Shin, Weiyan Ni, Xinqi Chen, Pengfei Ou, Yuan Liu, Neil M. Schweitzer, Debora Motta Meira, Vinayak P. Dravid, William A. Goddard, III, Ke Xie,* and Edward H. Sargent*

ACCESS | ⬛ Metrics & More | 📖 Article Recommendations | SI Supporting Information

ABSTRACT: The high carbon intensity of present-day ethylene glycol (EG) production motivates interest in electrifying ethylene oxidation. Noting poor kinetics in prior reports of the organic electrooxidation of small hydrocarbons, we explored the design of mediators that activate and simultaneously stabilize light alkenes. A ruthenium-substituted polyoxometalate (Ru-POM, $\{Si[Ru(H_2O)W_{11}O_{39}]\}^{5-}$) achieves 82% faradaic efficiency in EG production at 100 mA/cm^2 under ambient conditions. Via the union of *in situ* spectroscopic techniques, electrochemical studies, and density functional theory calculations, we find evidence of a two-step oxidation mechanism: Ru-POM first undergoes electrochemical oxidation to the high valent state, activating ethylene via partial oxidation and forming an intermediate complex; this intermediate complex then migrates to the anode where it undergoes further oxidation to produce EG. The Ru-POM-mediated electrocatalytic system reduces the projected energy consumption required in EG production, requiring 9 GJ per ton of EG (and accompanied by 0.04 ton H$_2$ coproduction), compared to 20−30 GJ/ton in typical prior processes.

$Si[Ru(H_2O)W_{11}O_{39}]^{-5}$
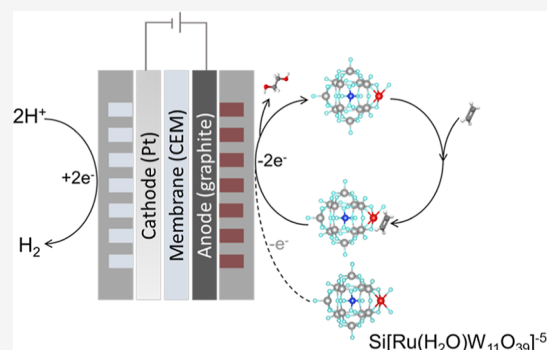
INTRODUCTION

Electrifying commodity chemical transformations offer one pathway to contribute to industrial decarbonization. The selective oxidation of hydrocarbons such as ethylene and propylene brings potential in light of present-day thermocatalytic transformations' large carbon footprint. Ethylene glycol (EG), for instance, with an annual global market exceeding 17 billion USD, has a carbon footprint of 55 million tons from present-day industrial processes.[1]

Recent efforts have led to major advances in ambient-temperature direct electrooxidation of olefins (eOOR).[2−4] Au-doped Pd achieved 80% faradaic efficiency (FE) in ethylene oxidation to EG at 6 mA/cm^2, while PdPtO$_x$ reached 66% FE in propylene oxidation to propylene oxide at 50 mA/cm^2 current density.[2,4] As yet, the direct approach has yet to achieve the union of high FE with >∼100 mA/cm^2 process intensity.

Mediated electrochemical systems may increase reactivity and thus partial current density by introducing a homogeneous process that addresses mass transfer limitations among gaseous reactants and solid electrodes.[5] Halide-mediated systems have showcased high FE, but the involvement of organohalogens motivates a search for additional options.[6]

We sought therefore to study redox-mediated routes to electrified organic oxidation, focusing on redox mediators that stabilize intermediates in small molecules such as ethylene, a challenging problem in light of limited resonance and charge distribution.

Transition metal oxides offering a ladder of available oxidation states have the potential to activate small hydrocarbon molecules and stabilize their intermediates.[7] The family of polyoxometalates (POMs), a polyatomic anion that consists of multiple transition metal oxyanions, seemed to us a class of redox mediator worth exploring.[8−10] POMs are typically composed of high oxidation state metal oxyanions, such as Mo(VI) and W(VI). While POMs and their derivatives have been studied for thermocatalytic alkene oxidation of relatively large molecules and aromatics, often requiring strong oxidants like persulfates, their application in electrocatalytic light olefin oxidation remains underexplored.[11]
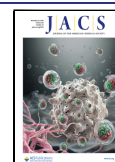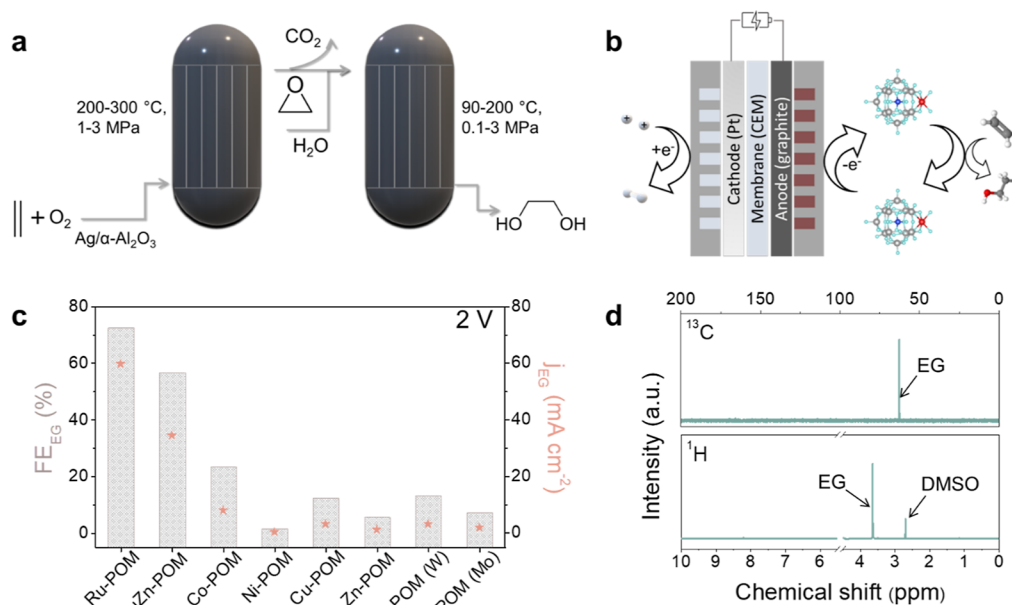
Figure 1. Ethylene oxidation and POM screening. (a) Present-day industrial ethylene oxidation (OOR) to EG; (b) shuttle system for eOOR explored herein; (c) POM screening; gray: FE of EG production; red: partial current density of EG production; (d) ^1H NMR and ^{13}C NMR of the analyte after OOR; DMSO was added as the internal standard to the post-reaction anolyte for the ^1H NMR quantification analysis. POMs screened are Ru-POM: $Si[Ru(H_2O)W_{11}O_{39}]^{5-}$; RuZn-POM: $\{[WZnRu_2(OH)(H_2O)](ZnW_9O_{34})_2\}^{11-}$; Co-POM: $P_2W_{18}Co_4(H_2O)_2O_{68}^{10-}$; Ni-POM: $[Ni(OH)_6W_6O_{18}]^{4-}$; Cu-POM: $P_2W_{18}Cu_4(H_2O)_2O_{68}^{10-}$; Zn-POM: $[WZn_3(H_2O)_2(ZnW_9O_{34})_2]^{12-}$; POM (W): $[SiW_{12}O_{40}]^{4-}$; POM (Mo): $[PMo_{12}O_{40}]^{3-}$.

POMs have shown promise in electrocatalytic applications including water oxidation reactions, where they have been used both as a catalyst and as redox mediator.[10,12] In one water-splitting system, silicotungstic acid served as a redox mediator, being reduced and protonated at the cathode before releasing hydrogen gas in a separate chamber.[8] POMs have demonstrated efficacy as redox mediators in electroorganic oxidation reactions (eOOR) such as the oxidation of alcohols and aromatic compounds.[13] These demonstrations, along with the programmable redox properties of POMs, motivated us to explore their potential as redox mediators for the eOOR of small olefins.

Here, we study POMs as redox mediators for eOOR, using ethylene oxidation as a model reaction. The Ru-substituted POM, $K_5Si[Ru(H_2O)W_{11}O_{39}]$, exhibits promising activity in ethylene oxidation to EG. Mechanistic studies suggest that Ru-POM serves not only as a redox mediator to activate ethylene through partial oxidation but also as a carrier, transporting the activated ethylene to the electrode for secondary oxidation to produce EG. We developed a reaction system that separates eOOR into two compartments: an electrolyzer where the POM is activated by losing electrons and an anodic reservoir where the activated POM reacts with ethylene. Through optimization of the catalyst and reactor design, we achieved near-unity total FE in ethylene oxidation to liquid products at 100 mA/cm², of which 82% FE toward EG production.

RESULTS AND DISCUSSION

Identifying Effective POMs for eOOR. To examine the feasibility of POMs in the electrified organic oxidation reaction (eOOR), we screened a series of POMs at 2 V using graphite felt as the anode (Figure 1c). Most POMs exhibited poor performance in terms of FE and current. We picture eOOR involving these steps: anodic redox mediator activation,

followed by the reaction between the activated redox mediator and ethylene. We hypothesize that the low FE in prior studies may have arisen because of different rates of these two processes: for example, too much oxidation of the redox mediator can trigger side reactions such as oxygen evolution and mediator degradation.

As a notable exception, Ru-POM ($K_5Si[Ru(H_2O)W_{11}O_{39}]$) achieved 72% FE at a 60 mA/cm² partial current density for ethylene-to-EG.

Ru-POM has historically demonstrated efficacy in thermocatalytic oxidation of long-chain and aromatic alkenes, but its performance with short-chain alkenes is unremarkable.[14−16] The existing routes to EG therefore rely instead on strong oxidation reagents, elevated temperatures, and high C_2H_4 partial pressure; these only resulted in a slow reaction rate and poor selectivity.

However, when we further optimized the Ru-POM eOOR system, we reached, at room temperature and pH 1, an 82% FE for EG and a production rate of ~40 kg_{EG} mol_{Ru}^{-1} h^{-1} at a current density of 100 mA/cm² (Figure S1). The major side product is formic acid (FA), the result of the overoxidation of EG. The combined faradaic efficiencies of EG and FA (FE_{EG+FA}) sum to 100 ± 2.5%. While formaldehyde could potentially form as a minor side product from the over-oxidation of EG, it is challenging to detect using our ^1H NMR method due to hydrate formation in an aqueous solution. However, given that the total FE of EG + FA approaches unity, we believe that formaldehyde production, if present, is minimal.

Mechanism Study of Ru-POM-Mediated eOOR. The encouraging performance of the best POMs in eOOR stimulated us to study the mechanism. We sought first to determine whether the Ru-POM anion cluster or dissociated free Ru ions, serves as the redox mediator. If Ru dissociates from the POM anion cluster, then adding extra POM
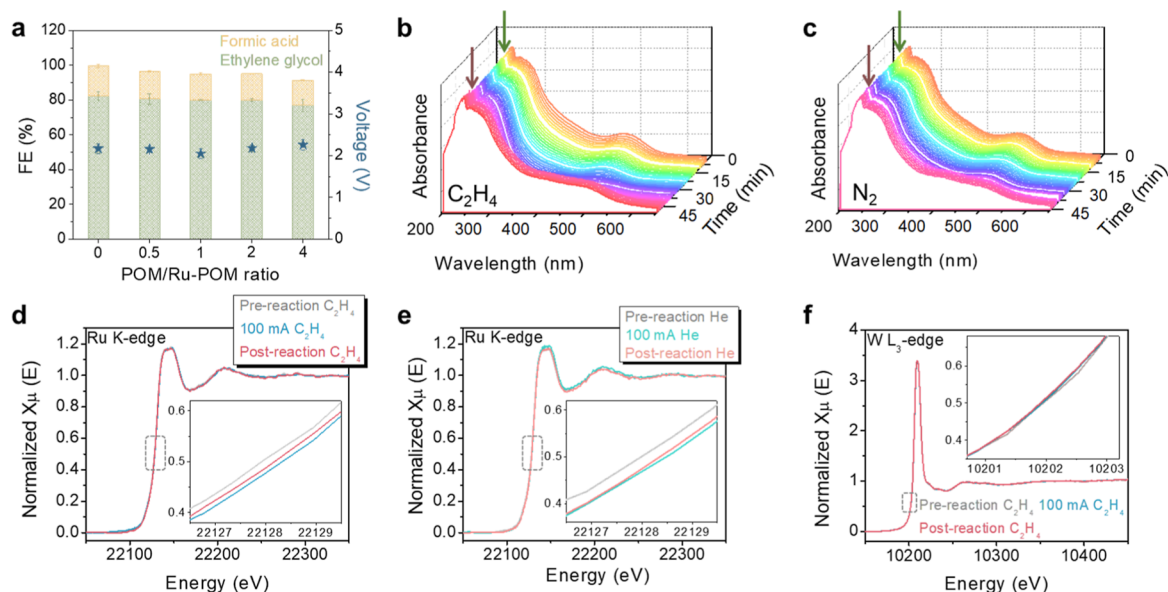
Figure 2. Study of redox chemistry in the eOOR system. (a) Performance of Ru-POM with extra POM in the system; the ratio of POM to Ru-POM is given as mass ratio. *In situ* UV−vis study of Ru-POM in the eOOR under (b) ethylene and (c) nitrogen; green arrow: start of current application at 100 mA/cm^2; brown arrow: cessation of current. *In situ* X-ray absorption near edge spectroscopy (XANES) study of (d) Ru K-edge during eOOR; (e) Ru K-edge during electrochemical oxidation under nitrogen; and (f) W L$_3$-edge during eOOR. Prereaction: spectrum obtained before applying current with continuous flow of C$_2$H$_4$ or He gas; 100 mA: spectrum obtained during eOOR with applied current at 100 mA; postreaction: spectrum obtained after stopping current while continuously flowing C$_2$H$_4$ or He gas.

(K$_8$SiW$_{11}$O$_{39}$) will shift the equilibrium, suppress Ru dissociation, and lower the abundance of free Ru ions in the system. If excess POM does not change ethylene oxidation performance in FE and full cell voltage, then Ru-POM is active as an anion cluster; otherwise, free Ru ions play a material role. As seen in Figure 2a, excess POM (up to 4 times the amount of Ru-POM) did not affect the activity of ethylene oxidation compared to pure Ru-POM: the 80% FE to EG and full cell voltage of 2−2.3 V were maintained.

Further experiments were conducted to test whether metal oxides resulting from the degradation of Ru-POM could serve as a catalyst (Figure S2).[17] We placed a suspension of RuO$_2$ in the electrolyte and also employed a RuO$_2$ electrode. The FE for EG in these tests (∼8%) was higher than the 4% FE observed in the reference experiment that used only graphite felt in a 0.1 M HClO$_4$ electrolyte. These values were 10× lower than the FE achieved in the Ru-POM reaction. We also considered the possibility that Ru^{3+} ions could function as catalysts in the electrolyte. Using RuCl$_3$ instead of Ru-POM at the same concentration resulted in an FE for EG of 28%, below the 82% FE with Ru-POM as the catalyst.

Looking at the reaction pathways, Ru-POM could act as an ethylene carrier by chemisorbing ethylene and transporting it to the anode for oxidation, though Ru(III) is not viewed as a good metal center for alkene activation in organometallic chemistry. Alternatively, Ru-POM could separate electrochemical redox chemistry and homogeneous ethylene oxidation to EG.

During eOOR, we observed that the color of Ru-POM in the anolyte changed from red-brown to midbrown, a qualitative hint of an oxidation state change in Ru. To quantify this change, we conducted *in situ* UV−vis spectroscopy on the ethylene oxidation system and also on a control case, the same system, but nitrogen-fed. According to literature reports, the peak centered at ∼480 nm corresponds to the oxidation state change of Ru.[18,19] Figure 2b and c demonstrates that when an

anodic current was applied, the intensity of the peak at 485 nm decreased, consistent with the oxidation of Ru(III). In the presence of ethylene, the 485 nm peak intensity began to recover when we removed the current. In contrast, no recovery was observed in the N$_2$ reference system.

From this, we hypothesize thus that Ru-POM first oxidizes at the anode (here we use Ru^O-POM to denote the oxidized form of Ru-POM, corresponding to species **2** in subsequent section) and Ru^O-POM then oxidizes ethylene, while Ru^O-POM is reduced back to the low oxidation state (Ru(III)-POM). A similar oxidation state change of Ru in Ru-POM was observed in *in situ* X-ray absorption spectroscopy (XAS), where Ru shifted to a higher oxidation state under the current and back to a lower oxidation state under ethylene (Figure 2d,e). In analogous studies on W, the major transition metal component in Ru-POM, we saw no evidence of an oxidation state change, suggesting that W is not the dominant redox chemistry center in Ru-POM (Figure 2f).

These results agree with a hypothesized mechanism in which Ru-POM first undergoes oxidation to a high oxidation state (Ru^O-POM) at the anode and then Ru^O-POM oxidizes ethylene while reverting back to its original state.

Ex situ X-ray photoelectron spectroscopy (XPS) on postreaction Ru-POM powder suggests the generation of Ru(IV) in the electrochemical oxidation process (Figures S3 and S4). However, in thermocatalytic oxidation, Ru-POM has previously been reported to be oxidized to a high oxidation state, Ru(V).[18]

To study further the redox chemistry of Ru-POM in the eOOR system, we conducted voltammetry studies in both single and flow cells. Cyclic voltammetry (CV) analysis in a three-electrode system with a glassy carbon disc working electrode exhibits two oxidation waves, one at 0.61 and the other at 0.89 V, under neutral conditions: we associate these with the redox couple Ru(III)/Ru(IV) and Ru(IV)/Ru(V) (Figure 3a).[19,20] When we titrate in HClO$_4$ to reach pH = 1.3,
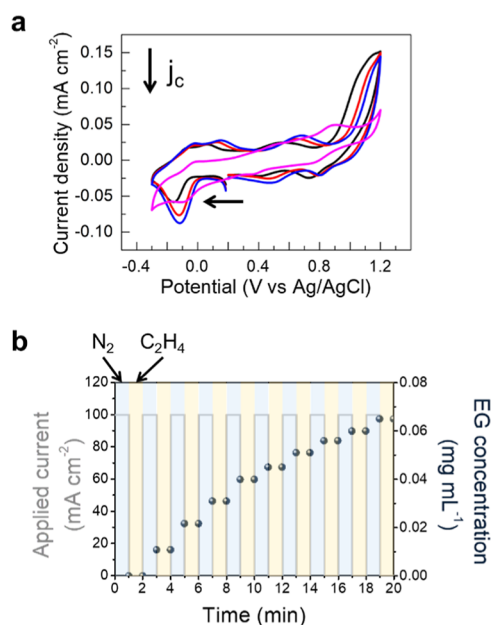
Figure 3. Mechanistic investigation of Ru-POM as a shuttle in eOOR. (a) CV of Ru-POM in pH = 7 (black), 1.3 (red), and 1.0 (blue) under N_2, and C_2H_4 (pH = 1.0. purple). Condition: single cell, with a glassy carbon disc electrode as a working electrode, Ag/AgCl (sat. KCl) as a reference electrode, and Pt wire as a counter electrode. (b) Current and ethylene flow pulse experiment; nitrogen was used to create an inert atmosphere during the application of a 100 mA/cm^2 current to the system. Ethylene flow was initiated after discontinuing the current. An additional 1 min nitrogen flow between ethylene flow and current initiation in nitrogen is not shown in the figure.

both oxidation peaks shift to more positive potentials, suggesting the protons are coupled with these redox events. The first oxidation is unchanged when we further adjust pH to 1, indicating that this oxidation proceeds without proton coupling, i.e., Ru(III)-OH$_2$ to Ru(IV)-OH$_2$. The second oxidation wave progressively shifts to more positive potential

as we lower pH to 1, which aligns with the formation of oxo or oxyl species. The second oxidation wave is irreversible under N_2; consistent structure change was indicated by IR, following electrolysis under a N_2 atmosphere. After purging with C_2H_4, only one set of redox peaks with $E_{p,a}$ = 0.9 V was observed in the range of 0.3−1.2 V vs Ag/AgCl (Figure 3a, purple line). In contrast to the CV curve under N_2, no secondary oxidation peak is present, suggesting a synergistic interaction between Ru-POM and ethylene that prevents further oxidation of Ru-POM to higher oxidation states. Further characterization indicates that the Ru-POM structure remains intact after electrolysis under C_2H_4, whereas it distinctly changes under N_2 (Figure S5). These structural observations align with the redox characteristics observed in the CV analysis.

During *in situ* UV−vis studies, as we examined the EG product, we noticed that the color of the anolyte progressively returned to its original state after the current was turned off. This suggested the recovery of Ru(III)-POM through the oxidation of ethylene. However, contrary to our expectations, the concentration of EG in the anolyte did not increase (refer to Figure S7).

This finding caused us to ask whether it might be direct oxidation of ethylene by Ru^O-POM that produces EG. We employed a pulsed experiment to explore the oxidation of ethylene to EG and elucidate the role of Ru-POM in this process. The experiment alternated between two phases (Figures 3b and S8): (1) applying current while purging the system with nitrogen (an inert gas), corresponding to blue regions; (2) halting the current while flowing ethylene through the system (yellow regions). If Ru(IV)-POM directly oxidized C_2H_4 to EG, then we would expect EG production during the ethylene flow periods. However, we observed that EG increases only when current was applied (blue regions). This suggests an additional electrochemical step in the ethylene-to-EG oxidation process. We propose that during the homogeneous redox process, a complex may form between Ru-POM and oxidized ethylene. This complex is then further oxidized at the anode when current is applied, resulting in the release of EG.
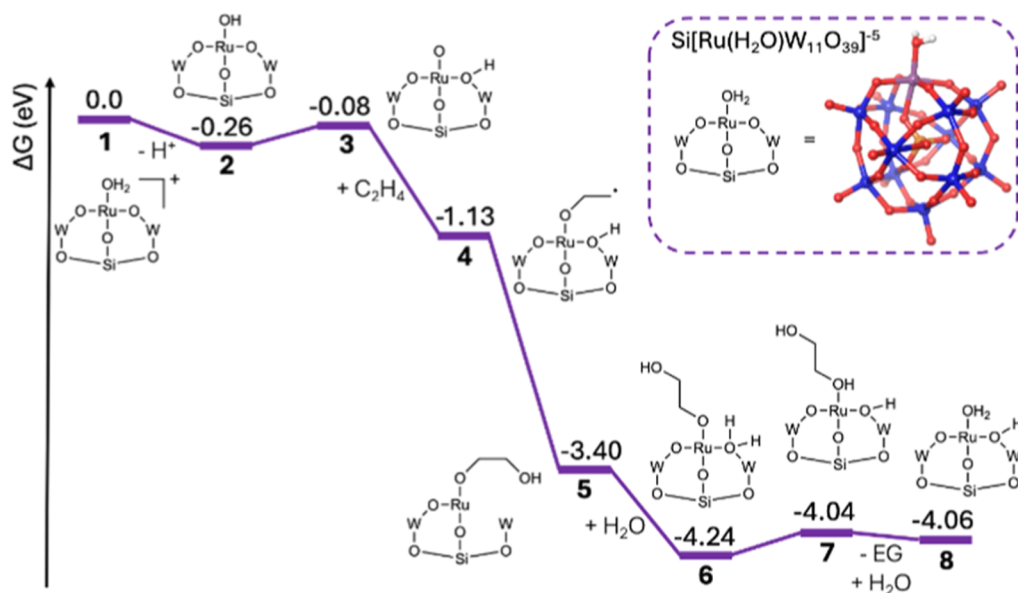

Figure 4. Free energy diagram for the electrocatalytic oxidation of ethylene to EG using Ru-POM. The reaction pathway shows the stepwise transformations of the Ru-POM species (1−8) during the catalytic cycle. Energy values are given in eV relative to the initial state.

Density functional theory (DFT) calculations were performed to further contemplate the reaction mechanism (Figure 4). Details of DFT methodology are given in Methods.

Previous studies suggest that beginning with Ru(III)-POM (henceforth Ru−H$_2$O), oxidation generates either singly oxidized [Ru−H$_2$O]$^+$ or doubly oxidized [Ru−H$_2$O]$^{+2}$. DFT predicts that single-electron oxidation occurs at +0.93 V vs RHE and two-electron oxidation at +1.29 V vs RHE, indicating that the singular oxidation to [Ru−H$_2$O]$^+$ is preferred. Following oxidation, deprotonation of [Ru−H$_2$O]$^+$ generates Ru-OH, which occurs with a ΔG of −0.26 eV. We hypothesize that the hydroxy moiety of Ru-OH is not sufficiently nucleophilic for readily oxidizing C$_2$H$_4$. Either the oxo or oxyl must be formed first, and these should be nucleophilic enough to oxidize C$_2$H$_4$ spontaneously. DFT predicts that the most probable route for oxo formation is via hydrogen migration from the hydroxy to a bridging oxygen (O$_b$), forming Ru−O−O$_b$H. Oxo formation via hydrogen migration occurs with a ΔG of +0.18 eV. Interception of C$_2$H$_4$ by Ru−O−O$_b$H results in direct C$_2$H$_4$ oxidation to afford Ru−OC$_2$H$_4$−O$_b$H; this step is downhill, −1.05 eV in free energy. The ensuing reaction step is oxidation of the −OC$_2$H$_4$ fragment to produce Ru−OC$_2$H$_4$OH. In alkaline media, this could occur in a straightforward manner via the reaction of Ru−OC$_2$H$_4$ with a solvated OH$^−$. However, our Ru-POM eOOR system operates optimally at pH = 1, such that the OH is alternatively sourced. DFT predicts the most exergonic route for OH addition to occur via coupling of the −OC$_2$H$_4$ and −O$_b$H ligands, which generates Ru-OC$_2$H$_4$OH with a ΔG of −2.27 eV. This coupling of −OC$_2$H$_4$ with −O$_b$H brings to mind prior mechanistic studies of heterogeneous ethylene oxidation in which a lattice OH reacts with adsorbed HOC$_2$H$_4$ to afford adsorbed EG.[2] OH addition renders a vacant site between Ru and neighboring W. DFT predicts the subsequent step to be insertion of a water into the said vacancy, which is downhill −0.84 eV and generates Ru−OC$_2$H$_4$OH−H$_2$O. To reoxidize the neighboring W, the inserted water now transfers an H to the −OC$_2$H$_4$OH, yielding Ru−HOC$_2$H$_4$OH−O$_b$H (ΔG = +0.20 eV). Finally, HOC$_2$H$_4$OH is displaced by water to afford the desired EG product and Ru−H$_2$O−O$_b$H. Oxidation of the −O$_b$H returns the catalyst to the Ru−H$_2$O starting state.

We present a picture (Figure 5), wherein Ru-POM acts as a dual shuttle in the eOOR process. In the scheme above, evidence from redox chemistry studies—including UV−vis spectroscopy, XAS, and pulse experiments—supports the involvement of a two-step oxidation process in eOOR. However, our conclusions regarding the oxidation state of the oxidized Ru-POM and the structure of reaction intermediates are based on indirect experimental evidence and theoretical studies. In this proposed mechanism, Ru-POM is first oxidized at the anode. In contrast with conventional strong-oxidant-assisted oxidation, controllable electrooxidation converts Ru(III) to Ru(IV). The Ru^O-POM (**2**) then acts as a homogeneous oxidant, and this partially oxidizes ethylene to generate an intermediate complex **4**. Transition metal oxyanions in Ru-POM provide charge-spreading by creating an electron deficient Ru center, thus stabilizing the complex for further oxidation. This complex then approaches the anode for secondary oxidation to produce EG. During the anodic oxidation of the complex, the Ru-POM undergoes reoxidation to Ru(IV) and the reaction cycle is thus completed.
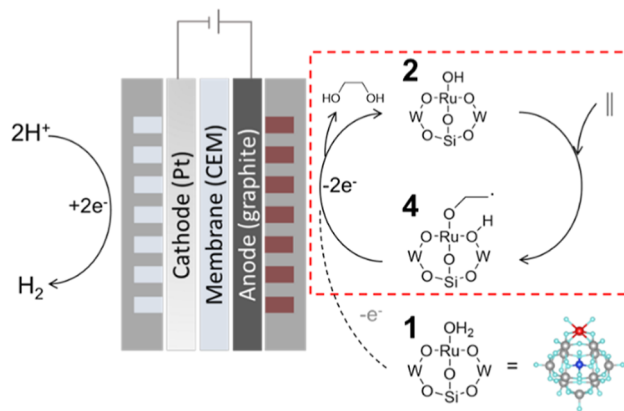

Figure 5. Proposed Ru-POM shuttle eOOR mechanism. Ru-POM first undergoes an oxidation process as shown via the dashed arrow, while the red square highlights the catalytic cycle. The structure of Ru^O-POM(**2**) and the intermediate complex(**4**) are proposed based on experimental and computational mechanistic studies.

While CV analysis and XPS characterization suggest an oxidation state of Ru(IV) for Ru^O-POM, we have yet to document direct confirmation. Due to the limitations in characterizing this system with electron-paramagnetic resonance (EPR) spectroscopy (Figure S9), we cannot definitively rule out the involvement of Ru(V)-oxo species in the reaction cycle. Additionally, alternative reaction pathways may be possible, such as ethylene chemisorption on Ru-POM followed by direct oxidation at the anode. These considerations underscore the need for further *in situ* studies to enhance understanding of the system.

Optimization of the Paired eOOR−Hydrogen Evolution Reaction Electrolyzer. We sought to pair eOOR with the hydrogen evolution reaction (HER), optimizing the reaction conditions. We varied the concentration of Ru-POM from 0.026 to 0.5 mM (Figure 6a) and found that even the lowest concentration of Ru-POM studied was capable of efficient eOOR. Higher Ru-POM concentrations lower the full cell voltage, but the FE to EG decreases from ∼82% to 74%, the result of incomplete usage of activated Ru-POM. We then paired HER with eOOR and focused on ≥100 mA/cm^2 current densities (Figures 6b and S10). Across a wide current range, the eOOR system demonstrated relatively high FE for ethylene oxidation. Focusing on the industrial scale current density of 100 mA/cm^2, we achieved 80% FE for EG production with a full-cell voltage of 2.2 V when paired with HER. The primary side product was FA, resulting from further oxidation. The combined FE of EG and FA (FE$_{EG+FA}$) approached unity (100 ± 2.5%) at the applied current density of 100 mA/cm^2. This corresponds to an energy intensity of 8.4 GJ/ton EG and a C.I. of 0.025 ton-CO$_2$/ton-EG (Figure 6c) when electricity having the carbon intensity of wind (11 g CO$_2$/kWh) is assumed. It is worth noting that the energy intensity of EG production from ethylene in this eOOR system is 3.5× lower than in the present-day industrial process and ∼1.5× below that of most energy-efficient prior electrified processes.

We recovered Ru-POM postreaction via precipitation by adding KCl and methanol (Figure S5). Characterization of the collected Ru-POM by using Raman spectroscopy and FTIR revealed no detectable structural changes. We carried out XRD, Raman spectroscopy, and scanning electron microscopy (SEM) studies of the postreaction electrode and did not find
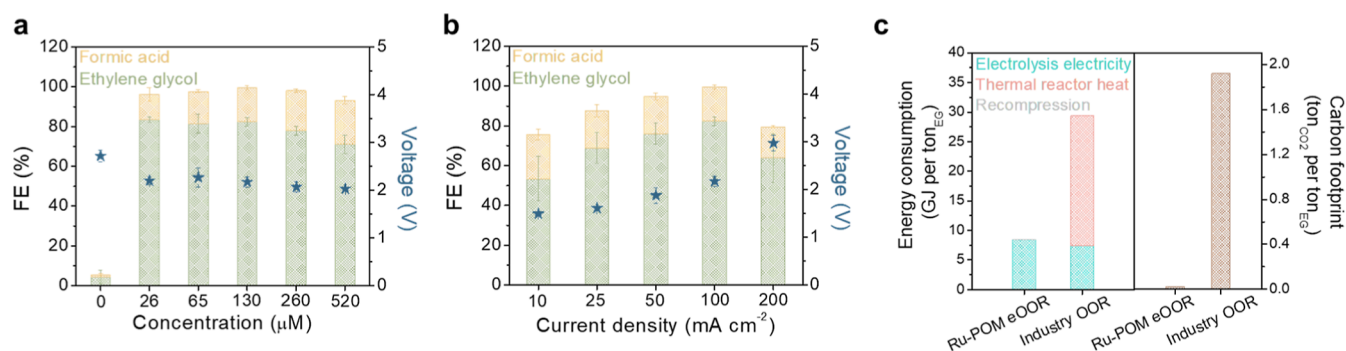
Figure 6. Performance evaluation of Ru-POM shuttled eOOR. FE and full cell voltage of electrocatalytic ethylene oxidation to EG with different (a) Ru-POM concentration; (b) current density. Panel (c) estimates the energy consumption and carbon intensity for Ru-POM shuttled eOOR vs present-day thermocatalytic ethylene to EG.

evidence of Ru-POM degradation nor metal oxide deposition (Figure S2).

CONCLUSIONS

The present study reports EG formation from ethylene using a ruthenium-substituted polyoxometalate (Ru-POM, $K_5Si[Ru(H_2O)W_{11}O_{39}]$)-mediated electrocatalytic system. Through *in situ* characterization, including UV–vis and XAS, we identify redox changes in Ru-POM, with electrochemical mechanistic studies indicating a two-step oxidation mechanism. The Ru center in Ru-POM is oxidized to a higher oxidation state at the anode and then partially oxidizes ethylene; partially oxidized ethylene is carried by Ru-POM to the anode for further oxidation, producing EG. In this process, Ru-POM serves as both a redox mediator and an ethylene carrier, forming a complex 4 with C_2H_4 that undergoes electrocatalytic oxidation to yield the final product. Based on this mechanistic understanding, we designed a flow electrolyzer system using a membrane electrode assembly setup and achieved 82% FE for EG production (the balance being 17% FE to FA) at a current density of 100 mA/cm². When paired with cathodic hydrogen evolution, the full cell voltage of the electrode is 2.2 V at 100 mA/cm².

METHODS

Materials. Sodium tungstate dihydrate (Na_2WO_4·$2H_2O$, 99+%, STREM chemicals, INC.), sodium metasilicate (Na_2SiO_3, Sigma-Aldrich), ruthenium chloride trihydrate ($RuCl_3$·$3H_2O$, Chem Scene), potassium chloride (KCl, 99+% ACS reagent, thermos scientific), hydrochloric acid (HCl, 36.5−38.0%, Fisher Chemical), perchloric acid ($HClO_4$, 70%, ACS reagent, Sigma-Aldrich), nitric acid (HNO_3, 68.0−70.0%, Fisher Chemical), phosphoric acid (H_3PO_4, ≥85 wt %, ACS reagent, Sigma-Aldrich), acetic acid (CH_3COOH, ≥99%, glacial, Sigma-Aldrich), deuterium oxide (D_2O, min. 99.9%, Sigma-Aldrich), dimethyl sulfoxide (DMSO, ≥99.9% anhydrous, Sigma-Aldrich), EG (≥99%, Sigma-Aldrich), zinc nitrate hexahydrate ($Zn(NO_3)_2$·$6H_2O$, 99%, Alfa Aesar), cobalt nitrate hexahydrate ($Co(NO)_2$·$6H_2O$, ≥98%, Sigma-Aldrich), nickel nitrate hexahydrate ($Ni(NO_3)_2$·$6H_2O$, 99.999% trace metal, Sigma-Aldrich), and copper nitrate trihydrate ($CuNO_3$·$3H_2O$, 99%, thermos scientific) were used as received. Milli-Q water (18.2 MΩ·cm at 25 °C) was used during all of the experimental procedures, including glassware cleaning and sample preparation.

Synthesis of $K_8[\alpha\text{-}SiW_{11}O_{39}]$·$13H_2O$. $K_8[\alpha\text{-}SiW_{11}O_{39}]$·$13H_2O$ was prepared by modifying a method reported in "inorganic synthesis".[21] Briefly, in a 250 mL round-bottom flask, 36.4 g of sodium tungstate (0.11 mol, Na_2WO_4·$2H_2O$) was dissolved in 60 mL of boiling water. 33 mL of 4 M HCl solution was slowly added to the boiling solution at the rate of 1 mL min⁻¹ controlled by a syringe

pump. A metasilicate solution, prepared by dissolving 2.2 g of sodium metasilicate (10 mmol, Na_2SiO_3) in 20 mL of water, was then added followed by a quick injection of another 10 mL of 4 M HCl solution. The solution was kept boiling for 1 h with reflux. After cooling to room temperature with a cold water bath, 30 g of KCl was added under stirring. The white precipitate was collected using centrifuge (7830 rpm, 7197g, 5 min) followed by washing with 10 mL of 1 M KCl solution twice and cold water once and finally dried under vacuum at room temperature. SEM images are shown in Figure S13.

Synthesis of $K_5Si[Ru(H_2O)W_{11}O_{39}]$ (Ru-POM). The preparation of $K_5Si[Ru(H_2O)W_{11}O_{39}]$ was performed following a previously reported method.[15,18,22] In a 70 °C oil bath, 1.5 g of prepared $K_8[\alpha\text{-}SiW_{11}O_{39}]$·$13H_2O$ was dissolved to 30 mL water in a 100 mL round-bottom flask. 0.15 g of $RuCl_3$·$3H_2O$ dissolved in the minimum amount of water was then added to the heteropolyanion solution dropwise, followed by refluxing at 70 °C for 60 min. The solution was cooled to 30 °C naturally when 10 g of KCl followed by 20 mL of methanol was added for precipitation. The brownish black precipitate was collected by centrifuging (7830 rpm, 7197g, 20 min), washed 3 times with a mixture of water and methanol (1:3 v/v), and dried under vacuum. Scanning transmission electron microscopy (STEM) images and energy-dispersive X-ray spectroscopy elemental mapping of Ru-POM before and after eOOR are shown in Figures S13 and S14.

Synthesis of Other Polyoxometalate. $Na_{11}\{[WZnRu_2(OH)(H_2O)](ZnW_9O_{34})_2\}$ were prepared using the previously reported method.[14,23] Briefly, $Na_{12}[WZn_3(H_2O)_2(ZnW_9O_{34})_2]$ was first prepared by adding $Zn(NO_3)_2$ solution into the acid-treated Na_2WO_4 solution at 90−95 °C.[24] Moderate cooling followed by liquid evaporation (50 °C, 3−4 days) yields needle-like crystals. The crystal was dried under a nitrogen flow at room temperature. The dichlorotetrakis (dimethyl sulfoxide) ruthenium complex ($RuCl_2(Me_2SO)_4$) was prepared by refluxing $RuCl_3$·$3H_2O$ in DMSO at 80 °C, precipitating and washing with acetone, and drying under vacuum.[25] The preparation of $Na_{11}\{[WZnRu_2(OH)(H_2O)](ZnW_9O_{34})_2\}$ included refluxing the mixture solution of $Na_{12}[WZn_3(H_2O)_2(ZnW_9O_{34})_2]$ and $RuCl_2(Me_2SO)_4$ under nitrogen, adding KCl for precipitation, and recrystallizing in hot water. After the second recrystallization, the prepared $Na_{11}\{[WZnRu_2(OH)(H_2O)](ZnW_9O_{34})_2\}$ was dispersed in hot water.

The preparation of $Na_4[Ni(OH)_6W_6O_{18}]$·$16H_2O$ was modified from a reported method.[26] To a 120 mL sodium tungstate solution (30 g, 0.091 mol, Na_2WO_4·$2H_2O$), 6 mL of 14 M HNO_3 was added under vigorously stirring. The mixture was kept at 85 °C until the formed yellow precipitate redissolved. 23 mmol of $Ni(NO_3)_2$ dissolved in 35 mL of water was added to the acid-sodium tungstate solution with 1 mL min⁻¹ adding rate at 95 °C. After staying at 95 °C for another 1−2 h, the mixture was filtered, and the clear blueish green filtrate was evaporated at 45 °C to yield blue crystals.

$K_{10}P_2W_{18}Co_4(H_2O)_2O_{68}$·$20H_2O$ and $K_7Na_3P_2W_{18}Cu_4(H_2O)_2O_{68}$·$20H_2O$ were prepared using a similar method.[27] $Na_8HPW_9O_{34}$ and Δ-$Na_8HPW_9O_{34}$ were first prepared by adding 0.75 mL 85% H_3PO_4 and

5.5 mL glacial acetic acid to 37 mL of sodium tungstate solution (30.0 g $Na_2WO_4 \cdot 2H_2O$) and collecting the precipitation. Δ-$Na_8HPW_9O_{34}$ was formed by simply heating $Na_8HPW_9O_{34}$ at 140 °C for 6 h. The synthesis of $K_{10}P_2W_{18}Co_4(H_2O)_2O_{68} \cdot 20H_2O$ involves refluxing Co-$(NO_3)_2$ and $Na_8HPW_9O_{34}$ under 140 °C, precipitation using KCl, and recrystallization at 5 °C. $K_7Na_3P_2W_{18}Cu_4(H_2O)_2O_{68} \cdot 20H_2O$ was synthesized by mixing $Cu(NO_3)_2$ with Δ-$Na_8HPW_9O_{34}$ at room temperature, KCl precipitation, and recrystallization with warm water at room temperature.

Electrocatalytic Ethylene Oxidation Evaluation. The electrocatalytic ethylene oxidation was evaluated in a membrane electrode assembly system (MEA). 1×1 cm^2 AvCarb G475A soft graphite battery felt (Fuel cell store), Nafion 117 (Fuel cell store), and Pt mesh folded to 2 layers (99.9%, 0.06 mm diameter, 0.12 mm thickness, Sigma-Aldrich) were used as anode, membrane, and cathode, respectively (the MEA setup shown in Figure S16). Anolyte was prepared by adding a certain amount of 20 mg mL^{-1} Ru-POM solution (200 mg of the as-prepared Ru-POM dissolved in 10 mL of H_2O) to 0.1 M $HClO_4$. Otherwise stated, the total amount of anolyte is 25 mL. Catholyte was 0.1 M $HClO_4$ solution. During a typical EO process, at room temperature, 50 SCCM C_2H_4 ($\geq$99.9%, UHP grade) was continuously bubbled into the anolyte (0.5 mL of 20 mg mL^{-1} Ru-POM added to 24.5 mL of 0.1 M $HClO_4$) through a glass felt. The anolyte was saturated with ethylene for 10 min. Then, the electrolyte was pumped through the MEA using peristaltic pumps with the flow rate of 45 mL min^{-1}. The EO was performed by applying current for 10 min. Another 10 min flowing of C_2H_4 after stopping the current allows for the completion of the eEO reaction. The liquid production analysis was conducted through nuclear magnetic resonance (NMR). Samples for NMR measurement were prepared by adding 50 μL of DMSO internal standard (1 mg mL^{-1}) and 50 μL of D_2O to 400 μL of anolyte. The calibration curve was generated for the quantitative analysis (Figures S17−S19).

The FE of the products was calculated using the following equation

$$FE = \frac{Q_{product}}{Q_{total}} \times 100\%$$

$Q_{product}$ charge consumed for product generation, in this case, EG or FA.

Q_{total} total charge passed during electrolysis.

For postreaction characterization, the Ru-POM concentration in the anolyte was increased to 2 mg mL^{-1} (650 mM). In the MEA system, a 2.2 V full cell voltage was applied for 1 h, while continuously flowing either ethylene or nitrogen through the anolyte. After terminating the application of voltage, we precipitated the postreaction Ru-POM by adding 5 g of KCl and 15 mL of methanol to the electrolyte. The precipitate was then centrifuged (7830 rpm, 7197g, 5 min) and washed three times with a mixture of water and methanol (5 mL of water with 25 mL of methanol). Following washing and centrifugation, the collected material was freeze-dried under a vacuum.

Cathode hydrogen evolution was quantified by using gas chromatography with a thermal conductivity detector (TCD). A continuous flow of 50 SCCM N_2 served as the carrier gas through a sealed catholyte reservoir. Hydrogen was the only gas product detected from the cathode with its FE approaching unity.

Gas product detection was performed using an online gas chromatograph (GC, Agilent GC 7890) equipped with a TCD and flame ionization detector (FID) (Jetanizer, ARC). Helium was used as the carrier gas. O_2 and N_2 were separated and detected with HP-Molesieve column (15 m $\times$ 0.530 mm $\times$ 50.0 μm) and TCD, while C_2H_4 and the other possible products including CO and CO_2, were separated with the HP-PLOT/Q column (30 m $\times$ 0.530 mm $\times$ 40.0 μm) and detected with FID (Figure S20).

The pulse experiment was conducted using 50 mL of anolyte consisting of 1 mL of a 20 mg mL^{-1} Ru-POM solution added to 49 mL of 0.1 M $HClO_4$. The MEA configuration and liquid flow rate were kept consistent with the standard eOOR process. The flow rates of N_2 and C_2H_4 were both set at 100 SCCM. Prior to initiating the

pulse experiment, the anolyte system underwent a 10 min N_2 purge. Next, a current of 100 mA/cm^2 was applied for 1 min. Following the 1 min current application under N_2, a 1 mL aliquot was extracted for NMR testing. Subsequently, the system was switched to pure C_2H_4 flow for 1 min, followed by another 1 min of N_2 flow. No current was applied to the system during these 2 min. After the N_2 flow, an additional 1 mL of aliquot was withdrawn. This 3 min cycle, comprising of current application, C_2H_4 flow, and N_2 flow, was repeated a total of 10 times.

The CV was performed by using a three-electrode flow cell system. Similar to the MEA system, the cathode, membrane, and anode consisted of Pt, Nafion 117, and graphite felt, respectively. An Ag/AgCl (saturated KCl) reference electrode was positioned between the membrane and anode. For the CV measurement, a voltage range of 0.54−1.54 V vs Ag/AgCl was applied, with a scanning rate of 50 mV s^{-1}. Throughout the CV test, both the anolyte (0.4 mg mL^{-1} Ru-POM in 0.1 M $HClO_4$) and catholyte (0.1 M $HClO_4$) were continuously flowed at a rate of 30 mL min^{-1}.

The CV test in a single cell was performed by using a three-electrode system. A glassy carbon electrode, Pt, and a Ag/AgCl (saturated KCl) electrode were used as the working, counter, and reference electrodes, respectively. The electrolyte consisted of a 2 mM Ru-POM solution. Prior to the CV test, the system was purged with 50 SCCM of either nitrogen or ethylene for 15 min. The gas inlet was then raised above the electrolyte surface. The CV scan began at 0.2 V, proceeded to −0.35 V, then to 1.2 V, and finally returned to 0.2 V, with a scan rate of 10 mV s^{-1}.

Characterization. High spatial resolution STEM characterizations were performed on a JEOL ARM 200CF microscope operated at 200 keV. This microscope was equipped with a probe corrector and dual silicon drift detectors. SEM was performed on a JEOL JSM-7900 FLV SEM. The Thermo Fisher Scientific NEXSA G2 XPS instrument was utilized to conduct an analysis of XPS. The analysis was performed by using an Al Kα monochromatic source with an X-ray spot size of 400 μm. An elemental scan was conducted with a passing energy of 50 eV and a step size of 0.1 eV. To calibrate the binding energies, the adventitious C 1s binding energy was fixed at 284.8 eV and used as an internal reference.

X-band continuous wave EPR spectra were recorded on a Bruker ESP 300 spectrometer equipped with an Oxford Instruments ESR 900 continuous He flow cryostat. The spectrum was collected under a temperature of 6 K.

***In Situ/Operando* Studies.** X-ray absorption near edge structure (XANES) measurements were made at beamline 20-BM at the Advanced Photon Source (APS) (Argonne National Laboratory, Argonne, Illinois) using a focused beam and a Si(111) double crystal monochromator. A Rh-coated mirror at 2 mrad and 15% detuning of the beam intensity were employed to promote harmonic rejection. Absolute energy calibration was made using Ru or W foil (edge energy of 22,117 eV and 10,207, respectively). The fluorescence was detected using a 7-element Ge detector at 90° to the beam direction. Details on the beamline optics and instruments can be found elsewhere.[28] A small reservoir ($\sim$1 mL liquid capacity) with a Kapton window for the *in situ* measurement was added between the anode and anode reservoir. Similar to the standard eEO experimental conditions, 50 SCCM ethylene or helium first flow through the primary reservoir for 30 min 100 mA/cm^2 current was applied for 30 min with continuous gas flowing. Gas flowed for another 30 min after the current stopped. During the whole 30 min process, the XAS spectrum was continuously obtained with $\sim$5 min for each spectrum. The spectra collected in the three regions (6−7 spectra for each step) were then merged to one spectrum and plotted into three curves, labeled as prereaction, 100 mA/cm^2, and postreaction.

The *in situ* UV−vis study was conducted on a spectrophotometer flow cell (10 mm path length, 15 mm dimension, 0.44 mL nominal volume, Starne Cells, Inc.) that connects the MEA anode and anode reservoir. Similarly, the standard conditions were applied during the *in situ* UV−vis study, while instead of 45 mL min^{-1} electrolyte flow, the flow rate reduced to 10 mL min^{-1} due to the flow limiting of the spectrophotometer flow cell. For the *in situ* UV−vis study under

ethylene, 100 mA/cm² current was applied for 30 min, while under N₂, 100 mA/cm² stopped after 15 min because the continuous consumption of Ru-POM leads to an increase in cell voltage and eventually voltage overrange stop. The UV−vis spectra were collected every 1 min.

COMPUTATIONAL METHODS

All DFT calculations were performed using the Jaguar v12.3 quantum chemistry software by Schrodinger Inc.[29] All calculations featured the M06-L density functional.[30] Light atoms (C, H, and O) were described with the 6-311G*+ basis set, while Ru and W were described by the Los Alamos large-core potential augmented with polarization and diffuse functions.[31] Implicit water solvation was utilized via Jaguar's Poisson−Boltzmann Finite Element solvation model.[32] Frequency calculations were performed to confirm that no imaginary frequencies were found as well as to predict thermochemical properties such as enthalpies, zero-point energies, and entropies. When Gibbs free energies were computed, translational and rotational entropies were reduced by 50% to account for librational modes hindered in solution. The water redox potential was assumed to be 4.66 V. The free energy of a solvated proton was assumed to be −265.9 kcal/mol.[33]

ASSOCIATED CONTENT

Supporting Information

The Supporting Information is available free of charge at https://pubs.acs.org/doi/10.1021/jacs.4c11891.

Additional discussion including the sample preparation for characterization and safety consideration; spectroscopic and microscopic characterizations of Ru-POM before and after eOOR; investigation of potential Ru-POM degradation; results of Ru-POM-mediated eOOR under different reaction conditions; scheme of paired HER-eOOR electrolyzer; process energy assessment; and eOOR performance comparison (PDF)

AUTHOR INFORMATION

Corresponding Authors

Ke Xie − Department of Chemistry, Northwestern University, Evanston, Illinois 60208, United States; orcid.org/0000-0003-4220-272X; Email: ke-xie@northwestern.edu

Edward H. Sargent − Department of Chemistry, Northwestern University, Evanston, Illinois 60208, United States; Department of Electrical and Computer Engineering, Northwestern University, Evanston, Illinois 60208, United States; orcid.org/0000-0003-0396-6495; Email: ted.sargent@northwestern.edu

Authors

Jiaqi Yu − Department of Chemistry, Northwestern University, Evanston, Illinois 60208, United States; orcid.org/0000-0001-7412-2746

Charles Bruce Musgrave, III − Department of Chemistry, Northwestern University, Evanston, Illinois 60208, United States; Materials and Process Simulation Center, California Institute of Technology, Pasadena, California 91125, United States

Qiucheng Chen − Department of Chemistry, Northwestern University, Evanston, Illinois 60208, United States

Yi Yang − Department of Chemistry, Northwestern University, Evanston, Illinois 60208, United States; orcid.org/0000-0002-7775-6856

Cong Tian − Department of Chemistry, Northwestern University, Evanston, Illinois 60208, United States; orcid.org/0000-0002-1260-3402

Xiaobing Hu − Department of Materials Science and Engineering and The NUANCE Center, Northwestern University, Evanston, Illinois 60208, United States; orcid.org/0000-0002-9233-8118

Guangcan Su − Department of Chemistry, Northwestern University, Evanston, Illinois 60208, United States; Department of Chemical and Biological Engineering, Northwestern University, Evanston, Illinois 60208, United States

Heejong Shin − Department of Chemistry, Northwestern University, Evanston, Illinois 60208, United States

Weiyan Ni − Department of Chemistry, Northwestern University, Evanston, Illinois 60208, United States; orcid.org/0000-0003-0234-4483

Xinqi Chen − Department of Mechanical Engineering, Northwestern University, Evanston, Illinois 60208, United States

Pengfei Ou − Department of Chemistry, Northwestern University, Evanston, Illinois 60208, United States; orcid.org/0000-0002-3630-0385

Yuan Liu − Department of Electrical and Computer Engineering, Northwestern University, Evanston, Illinois 60208, United States; orcid.org/0000-0001-8611-1673

Neil M. Schweitzer − Department of Chemical and Biological Engineering, Northwestern University, Evanston, Illinois 60208, United States; orcid.org/0000-0002-8284-6944

Debora Motta Meira − CLS@APS, Advanced Photon Source, Argonne National Laboratory, Lemont, Illinois 60439, United States; Canadian Light Source, Saskatoon, Saskatchewan S7N 2 V3, Canada; orcid.org/0000-0002-7529-2736

Vinayak P. Dravid − Department of Materials Science and Engineering and The NUANCE Center, Northwestern University, Evanston, Illinois 60208, United States; orcid.org/0000-0002-6007-3063

William A. Goddard, III − Materials and Process Simulation Center, California Institute of Technology, Pasadena, California 91125, United States; orcid.org/0000-0003-0097-5716

Complete contact information is available at:
https://pubs.acs.org/10.1021/jacs.4c11891

Author Contributions

♦J.Y., C.M., and Q.C. contributed equally.

Notes

The authors declare no competing financial interest.

ACKNOWLEDGMENTS

■ REFERENCES

(1) (a) Yang, Q.; Yang, Q.; Xu, S.; Zhu, S.; Zhang, D. Technoeconomic and environmental analysis of ethylene glycol production from coal and natural gas compared with oil-based production. *J. Cleaner Prod.* 2020, 273, 123120. (b) Xu, S.; Li, Z.; Yang, Q.; Chu, G.; Zhang, J.; Zhang, D.; Zhou, H.; Gao, M. Comparative Life Cycle Assessment of Energy Consumption, Pollutant Emission, and Cost Analysis of Coal/Oil/Biomass to Ethylene Glycol. *ACS Sustainable Chem. Eng.* 2021, 9 (47), 15849−15860.

(2) Lum, Y.; Huang, J. E.; Wang, Z.; Luo, M.; Nam, D.-H.; Leow, W. R.; Chen, B.; Wicks, J.; Li, Y. C.; Wang, Y.; et al. Tuning OH binding energy enables selective electrochemical oxidation of ethylene to ethylene glycol. *Nat. Catal.* 2020, 3 (1), 14−22.

(3) (a) Leow, W. R.; Völker, S.; Meys, R.; Huang, J. E.; Jaffer, S. A.; Bardow, A.; Sargent, E. H. Electrified hydrocarbon-to-oxygenates coupled to hydrogen evolution for efficient greenhouse gas mitigation. *Nat. Commun.* 2023, 14 (1), 1954. (b) Winiwarter, A.; Silvioli, L.; Scott, S. B.; Enemark-Rasmussen, K.; Sariç, M.; Trimarco, D. B.; Vesborg, P. C. K.; Moses, P. G.; Stephens, I. E. L.; Seger, B.; et al. Towards an atomistic understanding of electrocatalytic partial hydrocarbon oxidation: propene on palladium. *Energy Environ. Sci.* 2019, 12 (3), 1055−1067. (c) Li, A.-Z.; Yuan, B.-J.; Xu, M.; Wang, Y.; Zhang, C.; Wang, X.; Wang, X.; Li, J.; Zheng, L.; Li, B.-J.; et al. One-Step Electrochemical Ethylene-to-Ethylene Glycol Conversion over a Multitasking Molecular Catalyst. *J. Am. Chem. Soc.* 2024, 146 (8), 5622−5633. (d) Huang, J. E.; Chen, Y.; Ou, P.; Ding, X.; Yan, Y.; Dorakhan, R.; Lum, Y.; Li, X.-Y.; Bai, Y.; Wu, C.; et al. Selective Electrified Propylene-to-Propylene Glycol Oxidation on Activated Rh-Doped Pd. *J. Am. Chem. Soc.* 2024, 146 (12), 8641−8649.

(4) Chung, M.; Maalouf, J. H.; Adams, J. S.; Jiang, C.; Román-Leshkov, Y.; Manthiram, K. Direct propylene epoxidation via water activation over Pd-Pt electrocatalysts. *Science* 2024, 383 (6678), 49−55.

(5) Francke, R.; Little, R. D. Redox catalysis in organic electrosynthesis: basic principles and recent developments. *Chem. Soc. Rev.* 2014, 43 (8), 2492−2521.

(6) (a) Li, Y.; Ozden, A.; Leow, W. R.; Ou, P.; Huang, J. E.; Wang, Y.; Bertens, K.; Xu, Y.; Liu, Y.; Roy, C.; et al. Redox-mediated electrosynthesis of ethylene oxide from CO_2 and water. *Nat. Catal.* 2022, 5 (3), 185−192. (b) Leow, W. R.; Lum, Y.; Ozden, A.; Wang, Y.; Nam, D.-H.; Chen, B.; Wicks, J.; Zhuang, T.-T.; Li, F.; Sinton, D.; et al. Chloride-mediated selective electrosynthesis of ethylene and propylene oxides at high current density. *Science* 2020, 368 (6496), 1228−1233.

(7) (a) Ro, I.; Qi, J.; Lee, S.; Xu, M.; Yan, X.; Xie, Z.; Zakem, G.; Morales, A.; Chen, J. G.; Pan, X.; et al. Bifunctional hydroformylation on heterogeneous Rh-WO$_x$ pair site catalysts. *Nature* 2022, 609 (7926), 287−292. (b) Liu, J.; Ye, J.; Li, Z.; Otake, K.-i.; Liao, Y.; Peters, A. W.; Noh, H.; Truhlar, D. G.; Gagliardi, L.; Cramer, C. J.; et al. Beyond the Active Site: Tuning the Activity and Selectivity of a Metal−Organic Framework-Supported Ni Catalyst for Ethylene Dimerization. *J. Am. Chem. Soc.* 2018, 140 (36), 11174−11178.

(8) Rausch, B.; Symes, M. D.; Chisholm, G.; Cronin, L. Decoupled catalytic hydrogen evolution from a molecular metal oxide redox mediator in water splitting. *Science* 2014, 345 (6202), 1326−1330.

(9) (a) Yin, Q.; Tan, J. M.; Besson, C.; Geletii, Y. V.; Musaev, D. G.; Kuznetsov, A. E.; Luo, Z.; Hardcastle, K. I.; Hill, C. L. A Fast Soluble Carbon-Free Molecular Water Oxidation Catalyst Based on Abundant Metals. *Science* 2010, 328 (5976), 342−345. (b) Ai, F.; Wang, Z.; Lai, N.-C.; Zou, Q.; Liang, Z.; Lu, Y.-C. Heteropoly acid negolytes for high-power-density aqueous redox flow batteries at low temperatures. *Nat. Energy* 2022, 7 (5), 417−426. (c) Colliard, I.; Lee, J. R. I.; Colla, C. A.; Mason, H. E.; Sawvel, A. M.; Zavarin, M.; Nyman, M.; Deblonde, G. J.-P. Polyoxometalates as ligands to synthesize, isolate and characterize compounds of rare isotopes on the microgram scale. *Nat. Chem.* 2022, 14 (12), 1357−1366. (d) Amthor, S.; Knoll, S.; Heiland, M.; Zedler, L.; Li, C.; Nauroozi, D.; Tobaschus, W.; Mengele, A. K.; Anjass, M.; Schubert, U. S.; et al. A photosensitizer−polyoxometalate dyad that enables the decoupling of light and dark reactions for delayed on-demand solar hydrogen production. *Nat. Chem.* 2022, 14 (3), 321−327. (e) Zhao, T.; Bell, N. L.; Chisholm, G.; Kandasamy, B.; Long, D.-L.; Cronin, L. Aqueous solutions of super reduced polyoxotungstates as electron storage systems. *Energy Environ. Sci.* 2023, 16 (6), 2603−2610.

(10) Blasco-Ahicart, M.; Soriano-López, J.; Carbó, J. J.; Poblet, J. M.; Galan-Mascaros, J. R. Polyoxometalate electrocatalysts based on earth-abundant metals for efficient water oxidation in acidic media. *Nat. Chem.* 2018, 10 (1), 24−30.

(11) Weinstock, I. A.; Schreiber, R. E.; Neumann, R. Dioxygen in Polyoxometalate Mediated Reactions. *Chem. Rev.* 2018, 118 (5), 2680−2717.

(12) (a) Lei, J.; Yang, J.-J.; Liu, T.; Yuan, R.-M.; Deng, D.-R.; Zheng, M.-S.; Chen, J.-J.; Cronin, L.; Dong, Q.-F. Tuning Redox Active Polyoxometalates for Efficient Electron-Coupled Proton-Buffer-Mediated Water Splitting. *Chem. - Eur. J.* 2019, 25 (49), 11432−11436. (b) Martin-Sabi, M.; Soriano-López, J.; Winter, R. S.; Chen, J.-J.; Vilà-Nadal, L.; Long, D.-L.; Galán-Mascarós, J. R.; Cronin, L. Redox tuning the Weakley-type polyoxometalate archetype for the oxygen evolution reaction. *Nat. Catal.* 2018, 1 (3), 208−213. (c) Fabre, B.; Falaise, C.; Cadot, E. Polyoxometalates-Functionalized Electrodes for (Photo)Electrocatalytic Applications: Recent Advances and Prospects. *ACS Catal.* 2022, 12 (19), 12055−12091.

(13) (a) Stergiou, A. D.; Symes, M. D. Organic transformations using electro-generated polyoxometalate redox mediators. *Catal. Today* 2022, 384−386, 146−155. (b) Waldvogel, S. R.; Streb, C. Redox mediators facilitate selective electrocatalytic nitroarene-to-aniline reduction. *Chem* 2022, 8 (8), 2071−2073.

(14) Neumann, R.; Dahan, M. A ruthenium-substituted polyoxometalate as an inorganic dioxygenase for activation of molecular oxygen. *Nature* 1997, 388 (6640), 353−355.

(15) Neumann, R.; Abu-Gnim, C. A ruthenium heteropolyanion as catalyst for alkane and alkene oxidation. *J. Chem. Soc., Chem. Commun.* 1989, 18, 1324−1325.

(16) Liu, Y.; Zhao, S.-F.; Guo, S.-X.; Bond, A. M.; Zhang, J.; Zhu, G.; Hill, C. L.; Geletii, Y. V. Electrooxidation of Ethanol and Methanol Using the Molecular Catalyst $[\{Ru_4O_4(OH)_2(H_2O)_4\}(\gamma\text{-}SiW_{10}O_{36})_2]^{10-}$. *J. Am. Chem. Soc.* 2016, 138 (8), 2617−2628.

(17) (a) Folkman, S. J.; Soriano-Lopez, J.; Galán-Mascarós, J. R.; Finke, R. G. Electrochemically Driven Water-Oxidation Catalysis Beginning with Six Exemplary Cobalt Polyoxometalates: Is It Molecular, Homogeneous Catalysis or Electrode-Bound, Heterogeneous CoO$_x$ Catalysis? *J. Am. Chem. Soc.* 2018, 140 (38), 12040−12055. (b) Stracke, J. J.; Finke, R. G. Distinguishing Homogeneous

from Heterogeneous Water Oxidation Catalysis when Beginning with Polyoxometalates. *ACS Catal.* **2014**, *4* (3), 909−933.

(18) Neumann, R.; Abu-Gnim, C. Alkene oxidation catalyzed by a ruthenium-substituted heteropolyanion, SiRu(L)W11O39: the mechanism of the periodate-mediated oxidative cleavage. *J. Am. Chem. Soc.* **1990**, *112* (16), 6025−6031.

(19) Murakami, M.; Hong, D.; Suenobu, T.; Yamaguchi, S.; Ogura, T.; Fukuzumi, S. Catalytic Mechanism of Water Oxidation with Single-Site Ruthenium−Heteropolytungstate Complexes. *J. Am. Chem. Soc.* **2011**, *133* (30), 11605−11613.

(20) Sadakane, M.; Higashijima, M. Synthesis and electrochemical behavior of $[SiW_{11}O_{39}Ru^{III}(H_2O)]^{5-}$ and its oxo-bridged dimeric complex $[SiW_{11}O_{39}Ru^{IV}ORu^{III}SiW_{11}O_{39}]^{11-}$. *Dalton Trans.* **2003**, No. 4, 659−664.

(21) Téazéa, A.; Hervéa, G.; Finke, R. G.; Lyon, D. K. α-, β-, and γ-Dodecatungstosilicic Acids: Isomers and Related Lacunary Compounds. In *Inorganic Syntheses*; Wiley, 1990; pp 85−96.

(22) Filipek, K. Synthesis, characterization and reactivity of ruthenium complexes of the lacunary Keggin polyoxoanion: $[SiW_{11}O_{39}RuL]^{n-}$, L = H₂O, NO, N₂. *Inorg. Chim. Acta* **1995**, *231* (1−2), 237−239.

(23) Neumann, R.; Khenkin, A. M. Noble Metal (RuIII, PdII, PtII) Substituted ″Sandwich″ Type Polyoxometalates: Preparation, Characterization, and Catalytic Activity in Oxidations of Alkanes and Alkenes by Peroxides. *Inorg. Chem.* **1995**, *34* (23), 5753−5760.

(24) Tourné, C. M.; Tourné, G. F.; Zonnevijlle, F. Chiral polytungstometalates $[WM_3(H_2O)_2(XW_9O_{34})_2]^{12-}$ (X = M = Zn or Co^{II}) and their M-substituted derivatives. Syntheses, chemical, structural and spectroscopic study of some D,L sodium and potassium salts. *J. Chem. Soc., Dalton Trans.* **1991**, No. 1, 143−155.

(25) Evans, I. P.; Spencer, A.; Wilkinson, G. Dichlorotetrakis-(dimethyl sulphoxide)ruthenium(II) and its use as a source material for some new ruthenium(II) complexes. *J. Chem. Soc., Dalton Trans.* **1973**, No. 2, 204−209.

(26) Jin, P.; Wei, H.; Zhou, L.; Wei, D.; Wen, Y.; Zhao, B.; Wang, X.; Li, B. Anderson-type polyoxometalate as excellent catalyst for green synthesis of adipic acid with hydrogen peroxide. *Mol. Catal.* **2021**, *510*, 111705.

(27) Finke, R. G.; Droege, M. W.; Domaille, P. J. Trivacant heteropolytungstate derivatives. 3. Rational syntheses, characterization, two-dimensional tungsten-183 NMR, and properties of tungstometallophosphates $P_2W_{18}M_4(H_2O)_2O_{68}^{10-}$ and $P_4W_{30}M_4(H_2O)_2O_{112}^{16-}$ (M = cobalt, copper, zinc). *Inorg. Chem.* **1987**, *26* (23), 3886−3896.

(28) Heald, S. M.; Cross, J. O.; Brewe, D. L.; Gordon, R. A. The PNC/XOR X-ray microprobe station at APS sector 20. *Nucl. Instrum. Methods Phys. Res., Sect. A* **2007**, *582* (1), 215−217.

(29) Bochevarov, A. D.; Harder, E.; Hughes, T. F.; Greenwood, J. R.; Braden, D. A.; Philipp, D. M.; Rinaldo, D.; Halls, M. D.; Zhang, J.; Friesner, R. A. Jaguar: A high-performance quantum chemistry software program with strengths in life and materials sciences. *Int. J. Quantum Chem.* **2013**, *113* (18), 2110−2142.

(30) Zhao, Y.; Truhlar, D. G. The M06 suite of density functionals for main group thermochemistry, thermochemical kinetics, non-covalent interactions, excited states, and transition elements: two new functionals and systematic testing of four M06-class functionals and 12 other functionals. *Theor. Chem. Acc.* **2008**, *120* (1−3), 215−241.

(31) (a) Ditchfield, R.; Hehre, W. J.; Pople, J. A. Self-Consistent Molecular-Orbital Methods. IX. An Extended Gaussian-Type Basis for Molecular-Orbital Studies of Organic Molecules. *J. Chem. Phys.* **1971**, *54* (2), 724−728. (b) Roy, L. E.; Hay, P. J.; Martin, R. L. Revised Basis Sets for the LANL Effective Core Potentials. *J. Chem. Theory Comput.* **2008**, *4* (7), 1029−1031.

(32) Tannor, D. J.; Marten, B.; Murphy, R.; Friesner, R. A.; Sitkoff, D.; Nicholls, A.; Honig, B.; Ringnalda, M.; Goddard, W. A., III Accurate First Principles Calculation of Molecular Charge Distributions and Solvation Energies from Ab Initio Quantum Mechanics and Continuum Dielectric Theory. *J. Am. Chem. Soc.* **1994**, *116* (26), 11875−11882.

(33) Kelly, C. P.; Cramer, C. J.; Truhlar, D. G. Single-Ion Solvation Free Energies and the Normal Hydrogen Electrode Potential in Methanol, Acetonitrile, and Dimethyl Sulfoxide. *J. Phys. Chem. B* **2007**, *111* (2), 408−422.